The sodium/Na beta” alumina interface: Effect of pressure on voids

Dominic Spencer Jolly[a], Ziyang Ning[a], James E. Darnbrough[a,c], Jitti Kasemchainan[a,c], Gareth O. Hartley[a], Paul Adamson[a,c], David E.J. Armstrong[a,c], James Marrow[a], Peter G. Bruce[a,b,c]*

[a]Department of Materials, University of Oxford, Parks Road, Oxford OX1 3PH, UK

[b]Department of Chemistry, University of Oxford, South Parks Road, Oxford OX1 3QZ, UK

[c]The Faraday Institution, Harwell Campus, Didcot OX11 0RA

Keywords: solid-state battery, solid electrolyte, metal anode, interface, pressure dependence, X-ray tomography

Abstract:

3-electrode studies coupled with tomographic imaging of the Na/Na-β”-alumina interface reveal that voids form in the Na metal at the interface on stripping and they accumulate on cycling, leading to increasing interfacial current density, dendrite formation on plating, short circuit and cell failure. The process occurs above a critical current for stripping (CCS) for a given stack pressure, which sets the upper limit on current density that avoids cell failure, in line with results for the Li/solid-electrolyte interface. The pressure required to avoid cell failure varies linearly with current density, indicating that Na creep rather than diffusion per se dominates Na transport to the

interface and that significant pressures are required to prevent cell death, > 9 MPa at 2.5 mA·cm^{-2}.

1. Introduction

All-solid-state batteries (ASSBs) with a ceramic electrolyte and a metal anode promise to deliver improved safety as well as higher specific energies and energy densities compared with liquid electrolyte Li-ion batteries.[1–5] To date, Li metal anodes have garnered most attention due to their high theoretical capacity, 3860 mA·h·g^{-1}, versus 360 mA·h·g^{-1} for the graphite anode used in Li-ion cells. Na ASSBs, have received less attention due to their comparatively lower theoretical capacity (1166 mA·h·g^{-1}), despite still offering a significant improvement over hard carbon anodes used in Na-ion cells.[6] The Na/solid electrolyte interface offers an important comparison with the Li/solid electrolyte interface; the higher X-ray scattering of Na vs Li, makes operando tomographic studies of the evolving interface more tractable and studies of Na offer the prospect of better understanding the general aspects of alkali metal anodes in contact with ceramic electrolytes.[7]

Dendrite growth through the solid electrolyte at high current densities is a common failure associated with plating Li onto the Li anode at a high rate.[8–17] However, failures associated with stripping Li from the Li anode have only been recently characterised and show that Li metal mechanics are an important limiting factor on the rate at which Li can be stripped in an ASSB.[18] Koshikawa et al. used a 3-electrode cell to show that rapidly increasing Li/solid electrolyte interfacial impedance is a result of stripping rather than plating Li.[19] More recent studies of the Li/Li_6PS_5Cl (Argyrodite) interface by Kasemchainan et al., directly imaged voids at the interface of Li anodes and their accumulation on cycling, leading to contact loss, increase in local current density, dendrite formation on plating and cell death.[20] They also introduced the concept of a critical current density on stripping (CCS), dependent on pressure, above which voids will form and cells will die. As CCS is generally lower than the overall current density for dendrite formation on plating, it is often CCS that sets the maximum current density (rate) at which SSBs can operate. Krauskopf et al. imaged

void formation over a single charge under no pressure in a Li/$La_7La_3Zr_2O_{12}$/Li cell, linking the formation of these voids to an insufficient rate of diffusion in the lithium metal when cycled at current densities greater than 0.1 $mA \cdot cm^{-2}$.[21] Both papers note that anodic morphological stability is dependent on the rate of Li transport to the interface compared to the flux of Li-ions away due to current load and that the pressure dependence of morphological stability is due to the rate of stress-driven deformation (creep) of Li metal to the interface.

The mechanical properties of Na metal are different to those of Li.[22] In this work, we investigate the interface between Na metal and sodium beta alumina (Na-β"-alumina) through electrochemical and imaging techniques. Na-β"-alumina was chosen because it has a high conductivity (2 $mS \cdot cm^{-1}$) and is one of the most stable Na^+ ion conducting solid electrolytes known.[23–25] Dendrite formation has been reported for Na beta alumina in contact with molten Na.[26–28] Here, we demonstrate void accumulation on cycling that is similar to the Li/solid electrolyte interface.[15,18,20,21] In addition, we image directly, *in operando*, the coalescence of voids on cycling using tomography. We also determine the functionality of interfacial contact loss with pressure and show that the critical pressure above which voids do not form and hence cells do not die varies linearly with the current density of cell operation. The results show that creep and plastic deformation rather than diffusion dominate Na transport to the interface.

2. Results and Discussion

Alkali rich oxides invariably have hydroxides and carbonates present on their surfaces. Such contaminants can have a significant effect on the interface with alkali metals.[29–32] Disks of Na-β''-alumina (Ionotec), 10 mm diameter and 0.7 mm thick, >96 % dense were subjected to a similar procedure to that described recently by Sakamoto and co-workers for the removal of hydroxide and carbonate surface species from $La_7La_3Zr_2O_{12}$ (LLZO) disks, involving a polishing and heating protocol.[29] The surface treatment was found to reduce greatly the interfacial impedance of Na/Na-β''-alumina/Na cells when examined by X-ray photoelectron spectroscopy (Supplementary Figure 1) and AC impedance spectroscopy (Supplementary Figure 2), consistent with the reduction in surface hydroxide and carbonate species on the surface of the oxide. All procedures are described in Methods.

In a 2-electrode cell, current is passed between the working and counter electrodes and the voltage response between these electrodes is measured. In this study, 3-electrode cells were also used in which the voltage is instead measured between the working electrode and an added reference electrode. As a result, the voltage response is due to changes occurring solely at the working electrode, allowing for the differentiation between the processes of stripping and plating. 3-electrode cells were constructed as described in the Method section, using Na metal foil as the working, counter and reference electrodes as shown in Supplementary Figure 3. The cell was placed under a constant pressure which was controlled throughout cycling as also described in Methods. Constant current was passed between the working and counter electrodes whilst the potential was simultaneously measured between the working and reference electrodes and between the counter and reference electrodes. Cell cycling began by plating on the working electrode (and stripping the counter electrode) followed by stripping the working electrode (and plating the counter electrode). A capacity of 0.5 $mA \cdot h \cdot cm^{-2}$ was cycled, equivalent to stripping/plating approximately 5 μm of Na.

We first report the 3-electrode cycling behaviour of cells cycled under 4 MPa pressure, using cross-sectional SEM and X-ray tomography to explain the mechanical changes associated with stripping and

plating. Having established this, we report the differences of cycling under the higher pressure of 7 MPa before discussing asymmetries between the working and counter electrodes and establishing a method for determining the critical pressure for stable cycling of the Na metal anode for a range of current densities.

2.1. Cycling 3-electrode cells under 4 MPa of pressure

Cycling under a pressure of 4 MPa at a current density of 1.5 $mA \cdot cm^{-2}$ results in a marked asymmetry between plating and stripping, the former exhibits a very low and constant polarisation (12 mV) with charge passed on each cycle, whereas polarisation is observed to increase with charge passed on stripping and to increase with cycle number from 0.23 V in cycle 1 to 0.42 V in cycle 10 (Fig 1a). These results for a sodium metal/sodium ion solid electrolyte interface are in good accord with those published recently by us on the Li/Li_6PS_5Cl interface, where increased polarisation on stripping with cycling was attributed to void formation that worsens with cycle number, decreasing the true area of contact between SE and Na electrode.[20]

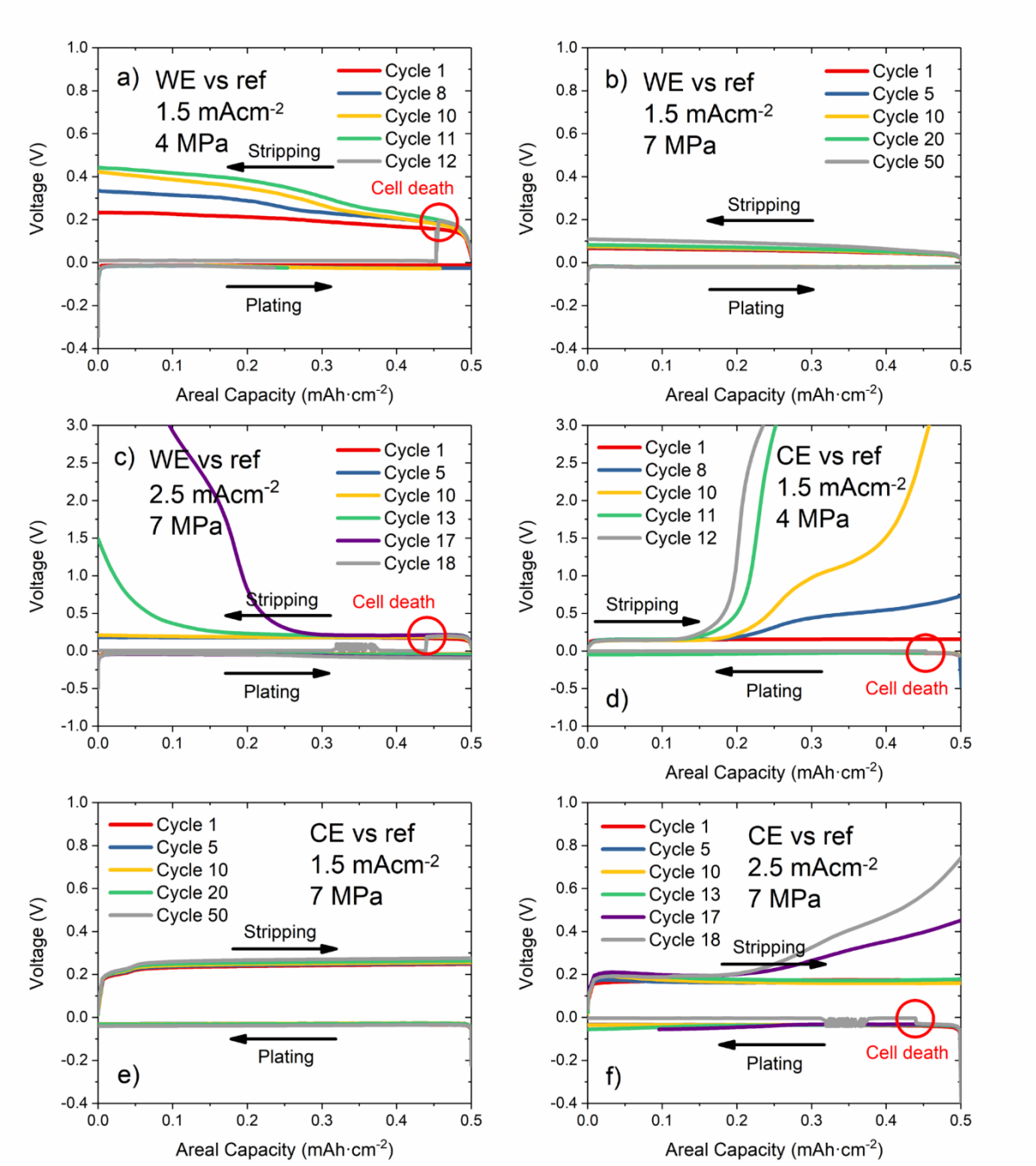

Figure 1: Voltage measured between working and reference electrodes when cycling at a) 4 MPa and 1.5 mA·cm^{-2} b) 7 MPa and 1.5 mA·cm^{-2} and c) 7 MPa and 2.5 mA·cm^{-2} and measured between counter and reference electrodes at d) 4 MPa and 1.5 mA·cm^{-2} e) 7 MPa and 1.5 mA·cm^{-2} and f) 7 MPa and 2.5 mA·cm^{-2}. WE, CE and ref are the working, counter and reference electrodes respectively.

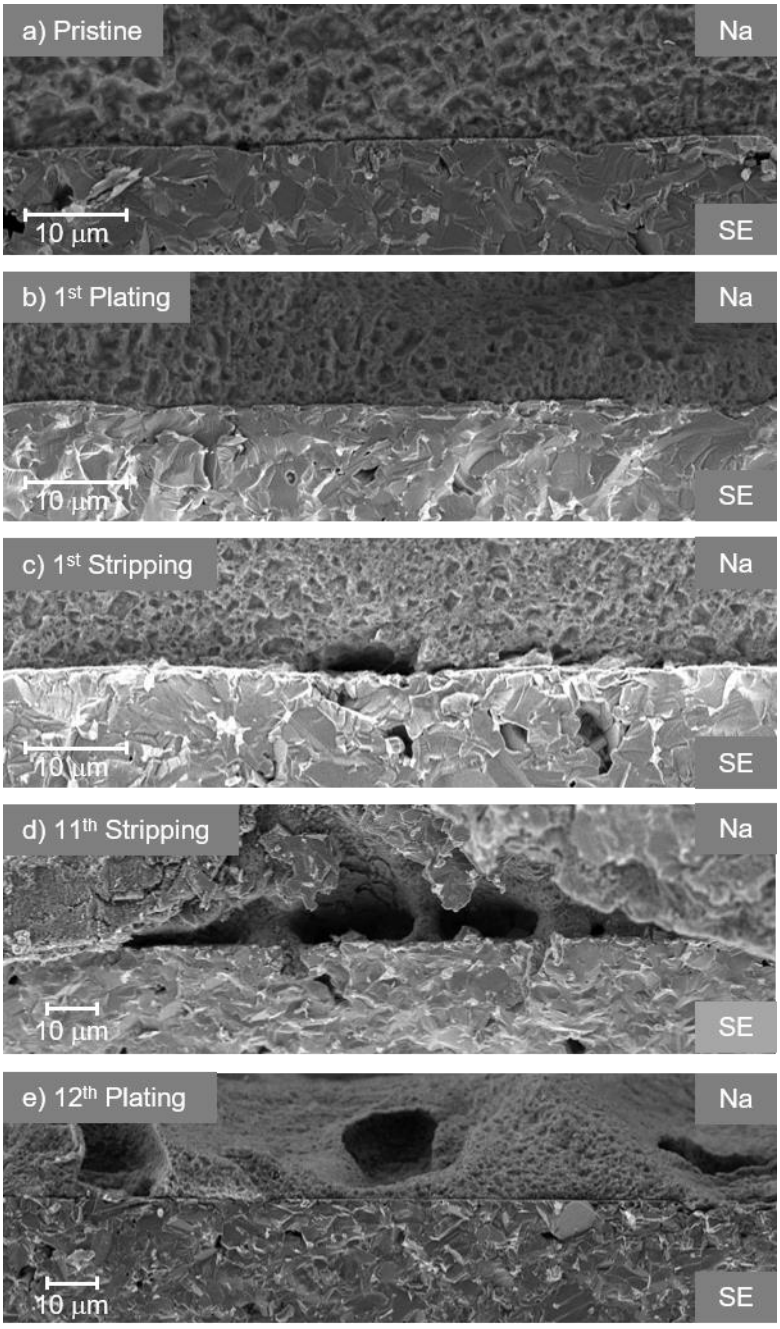

Figure 2: Cross-sectional SEM images of the Na/Na-β"-Al_2O_3 interface when a) pristine and after b) 1st plating c) 1st stripping d) 11th stripping and e) 12th plating after cycling under 4 MPa pressure at 1.5 mA·cm^{-2}

To confirm the origin the asymmetry between stripping and plating, 3-electrode cells cycled under a pressure of 4 MPa at a current density of 1.5 mA·cm^{-2} with a capacity of 0.5 mAh·cm^{-2} were disassembled and cross-sectioned as described in the Methods and their interfaces imaged by SEM. These results are shown in Figure 2.

The micrographs of the Na/Na Na-β"-alumina interface confirm the asymmetry between stripping and plating observed in the electrochemistry is due to void formation during stripping and the rapid healing of the interface on plating.

2.1.1. Stripping

After the first plating (Fig 2b), the interfacial morphology looks much like in the pristine cell (Fig 2a) with no voiding evident. However, following the first stripping small voids are observed at the interface (Fig 2c). This is consistent with the conclusion from the 3-electrode cycling data (Fig 1a) and previous literature that void formation is a phenomenon that occurs on stripping. A comparison between the interfaces following the first stripping and the final stripping (Fig 2d) clearly show that voids grow significantly in size over successive cycles which is in agreement with the polarisation increase observed in Fig 1a.

In previous work we identified the critical current density on stripping (CCS) as the current density above which voids will form at the interface.[20] CCS is defined as the current density above which Na metal is stripped at a faster rate than it can be replenished at the Na/SE interface. Therefore, the condition for void formation on stripping is as described in Equation 1:

$$Rate\ of\ Na\ diffusion + Rate\ of\ stress\ driven\ deformation\ <\ Ion\ flux \qquad (1)$$

In the case of a cell cycled at 1.5 $mA \cdot cm^{-2}$ under a 4 MPa pressure, it is clear that the rate of Na^+ flux away from the interface exceeds the rate of replenishment at the interface i.e. 1.5 $mA \cdot cm^{-2}$ > CCS. This leads to the development of voids on stripping and eventual cell death.

2.1 2. Plating

Just as for Li/Li_6PS_5Cl, the polarisation on plating is observed to remain low and relatively constant, suggesting the reformation of a conformal interface with each plating. The micrograph showing the final plating offers some insight (Fig 2e), clearly showing a conformal interface but also voids in the Na which are set back from the interface. On plating Na, the metal will nucleate at the most energetically favourable point. When there is a pre-existing void at the interface, this point of nucleation will be the triple point between SE, Na and void, since the Na nucleus does not have to push against the pressure to create volume in order to grow. Growth of Na will occur across the solid electrolyte interface forming a thin film with only a small quantity of charge passed, explaining the low polarisation on plating and at a value very similar

to that on the first plating. The result of such lateral Na growth is that only some of the voids present on the previous stripping are filled in, others are occluded and pushed back from the Na/SE interface as Na plating continues. This process is shown in Figure 3. The thin Na film and occlusion of voids are evident in the image in Fig 2 (e). These observations are in line with those for Li/Li_6PS_5Cl.[20]

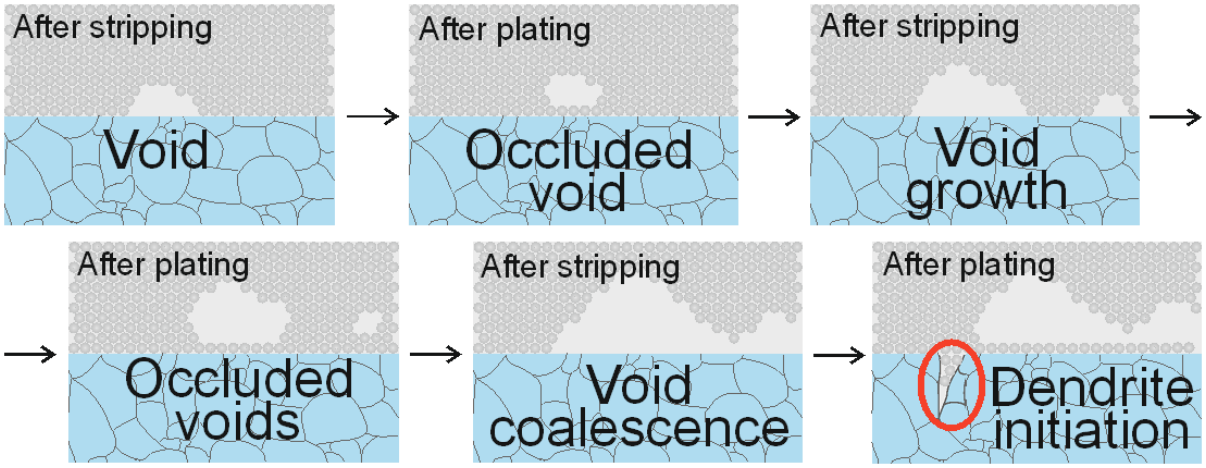

Figure 3: Schematic showing the mechanism for voiding and eventual dendrite growth. Grey represents the sodium electrode and blue the Na-β"-alumina

2.1.3. The evolution of voids on cycling: Operando X-ray Tomography

The non-destructive nature of tomography means that changes at the interface can be followed without any uncertainties from the effect of physical sectioning. Operando X-ray tomography was performed to observe how the voids grow and evolve on cycling. The higher X-ray scattering of Na compared to Li enables higher contrast, clearer imaging of the interface, giving new key insights into void development. Figure 4 shows images of a cell at key points in cycling; when pristine and after 1st stripping, 1st plating, 2nd stripping, 2nd plating, 3rd stripping, 3rd plating, 4th stripping and 4th plating.

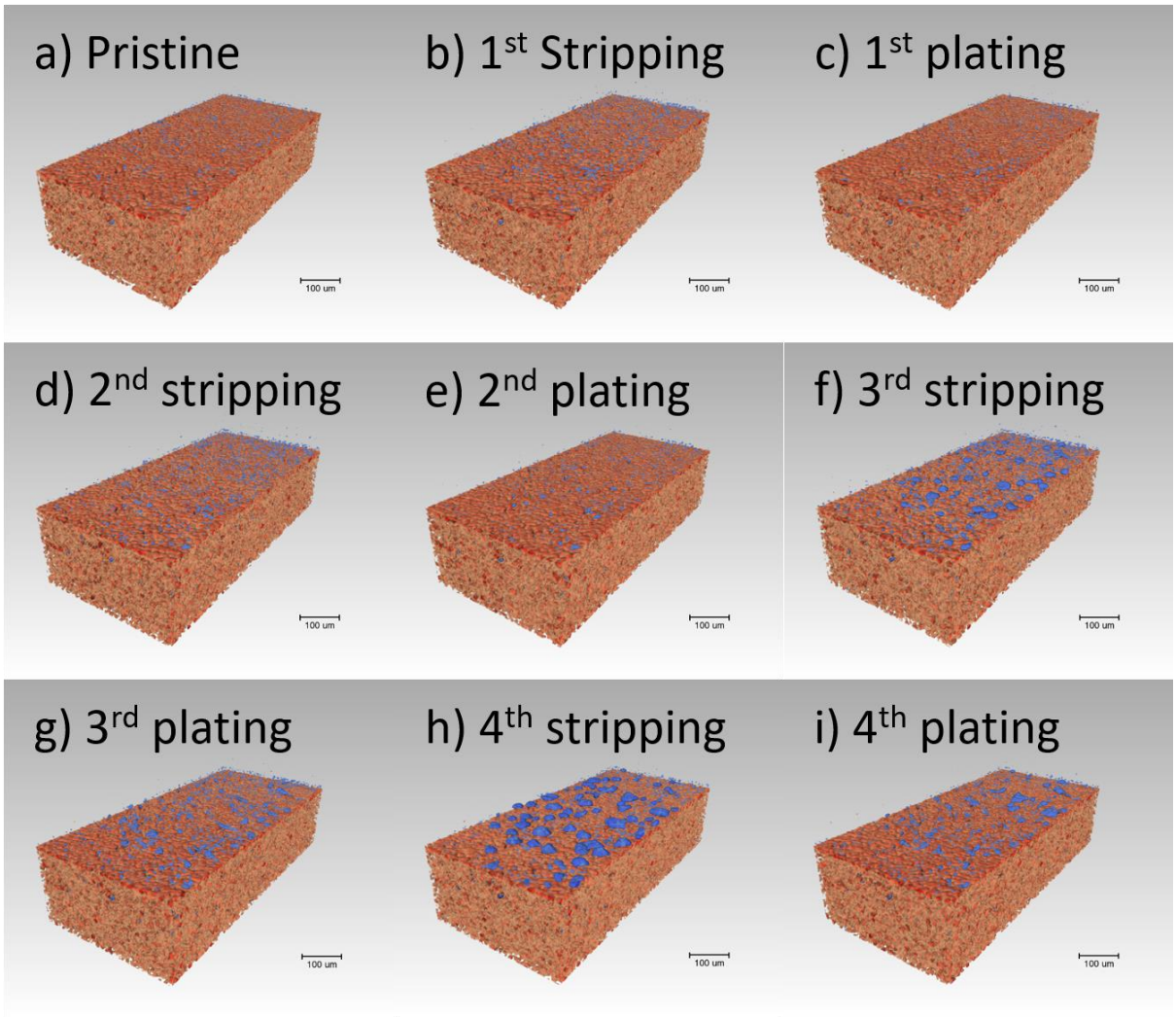

Figure 4: X-ray tomography images of the Na/Na beta alumina interface when a) pristine and after b) 1st stripping c) 1st plating d) 2nd stripping e) 2nd plating f) 3rd stripping g) 3rd plating h) 4th stripping and i) 4th plating. Orange indicates solid electrolyte and blue indicates voids in the sodium anode (transparent). The cell was cycled at a pressure of 2 MPa and a current density of 1.5 $mA \cdot cm^{-2}$ with a capacity of 0.75 $mA \cdot h \cdot cm^{-2}$.

The Operando X-ray tomography reveals the following key insights:

1. Small voids are present even at the pristine interface (Fig 4a), indicative of some porosity in the Na metal itself.

2. Voids increase in number and size on stripping and diminish in number and size on the subsequent plating, in agreement with previous theory.[20]
3. Voiding at the interface increases as a function of cycle number, supporting the conclusions made by SEM of the interface (Fig 2).

The tomographic results can be analysed quantitatively by determining the number and volume of voids (as described in Methods) and how this evolves on cycling. An analysis of the total volume of voids at different stages of cycling is presented in (Fig 5a). The volume of voids at the end of each stripping increases as a function of cycle number, consistent with increasing detachment. This is particularly clear from the 3rd stripping. The voids are only partially filled on subsequent plating, as is evident from cycle 3 onwards. The void volume at the end of each plating also increases on cycling, in accord with increasing volume of occluded voids.

Figure 5b shows the number of voids in three different size regions. It is evident that larger voids become more apparent at higher cycle number. The small voids (1000-2500 μm^3) dominate on the 2nd stripping. Interestingly, despite the appearance of the medium (2500-10000 μm^3) and large voids (>10000 μm^3) at higher cycle numbers, the small voids persist on stripping and crucially also on plating. This implies that as the larger voids are filled in on plating, such filling is not complete in many cases, resulting in smaller voids at the end of plating.

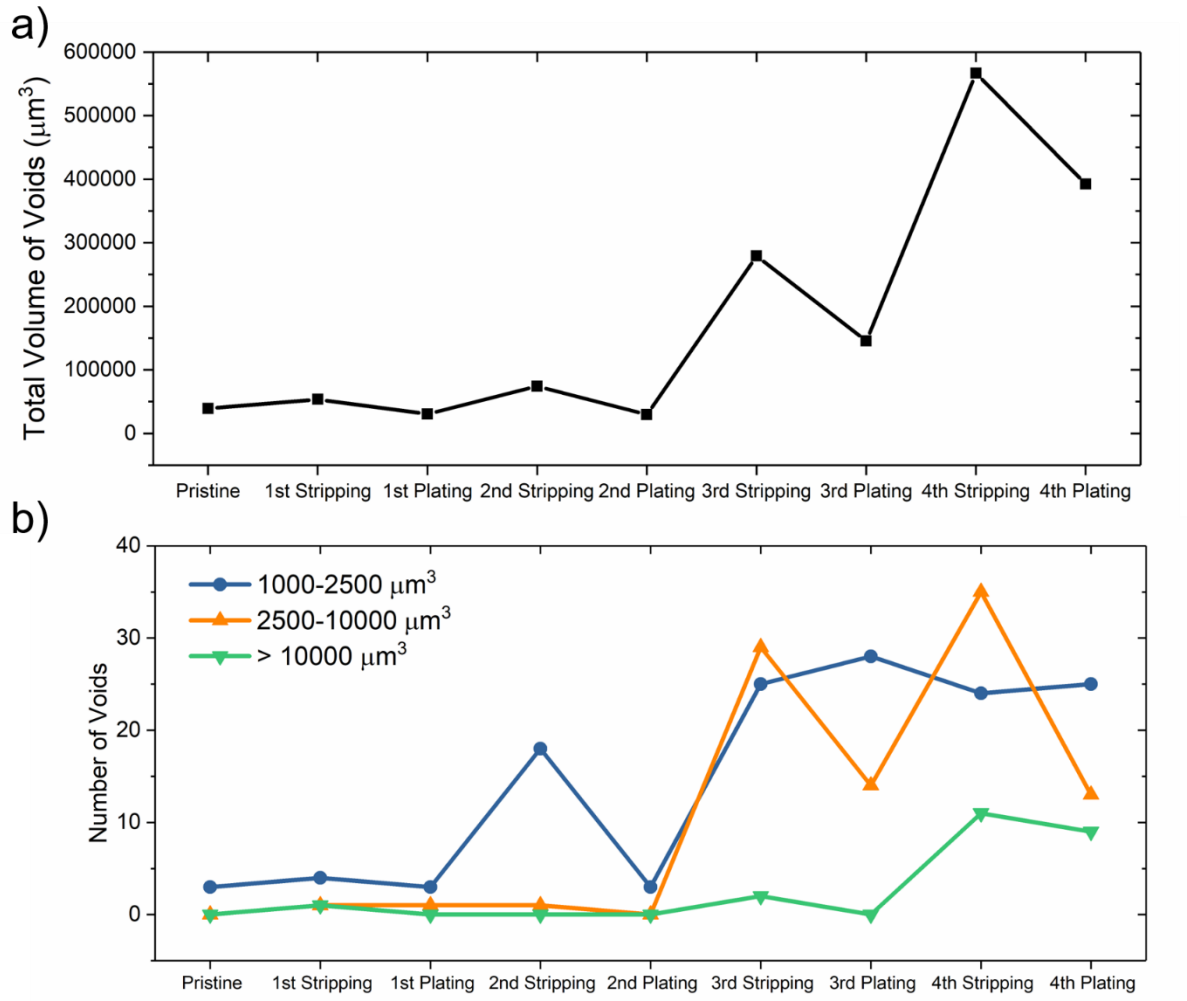

Figure 5: Plots showing (a) The total volume of voids in the Na anode and (b) The number of voids in the range 1000-2500 µm^3 (blue), 2500-10000 µm^3 (orange) and >10000 µm^3 (green). Analysis was performed on a 6.58×10^{-2} mm^3 volume of the cell interface.

As a result, when cycling above CCS, voids will initiate at the interface and grow in size and accumulate with cycle number. The local current density varies with the true area of contact between electrode and electrolyte as described in Equation 2.

$$I_{local} = {I_0}\Big/{\left(\frac{A}{A_0}\right)} \qquad (2)$$

where I_{local} is the local current density, I_0 is the applied current density (assuming 100 % contact), A is the true area of contact and A_0 is the area given 100 % contact.

As Figure 5 shows, the total volume of voids increases with cycle number. This is accompanied by a decrease in the area of contact at the Na/Na-β"-alumina (A). Therefore, when cycling above CCS, contact loss will become great enough that there are high local plating currents (I_{local}). This will result in dendrite growth and cell death as observed in the 12th cycle of Fig 1a.

2.2. Cycling 3-electrode cells under 7 MPa of pressure

The effect of pressure is reported in Fig 1b, where cycling was carried out at the same current density as in Fig 1a (1.5 mA·cm^{-2}) but at the higher pressure of 7 MPa. A low polarisation is again observed on plating. However, a much smaller increase in polarisation is observed on stripping, remaining low over 50 cycles (Fig 1b). Such a cell was cross-sectioned and imaged by SEM at three points during cycling (Supplementary Figure 4a). The micrographs show a morphologically stable interface following the 1st stripping, the 25th stripping and the 50th stripping, consistent with the electrochemical observation of stable potential. This suggests that there is little or no decrease in the true area of contact between the SE and Na electrode at 7 MPa, meaning that the higher pressure does indeed suppress void formation.

Increasing the current density to 2.5 mA·cm^{-2} at the same high pressure of 7 MPa again showed polarisation on stripping that increases greatly with cycle number, reaching 3.0 V in cycle 17 before the cell short-circuited (Fig 1c). As such, the cycling data showed similarities to that at a current density of 1.5 mA·cm^{-2} under a 4 MPa pressure. As before, there was an increase in polarisation with subsequent strippings, suggesting the formation and accumulation of voids until the cell fails on the 18th cycle. A SEM of the interface following cell death confirmed the conclusion that there was significant voiding at the interface (Supplementary Figure 4b). It can therefore be concluded that at a pressure of 7 MPa, 2.5 mA·cm^{-2} is >> CCS.

2.3. Counter electrode vs reference electrode

The polarisation of the working and counter electrodes vs the reference were collected simultaneously. The data for the counter electrode from the same cells and cycling experiments as in Fig 1 a to c are shown in Fig 1 d to f. As expected, the cell which was cycled for 50 cycles without failure (1.5 $mA \cdot cm^{-2}$ under 7 MPa pressure) showed no large increase in polarisation on stripping or plating at the counter electrode (Fig 1e), just as for the working electrode vs reference. The two cells which showed increasing polarisation on stripping at the working electrode and failed (1.5 $mA \cdot cm^{-2}$ under 4 MPa pressure and 2.5 $mA \cdot cm^{-2}$ under 7 MPa pressure) both show no increase in polarisation on plating but an increase in polarisation with cycle number on stripping just as for the working electrode. However, it is striking that the increase in polarisation on stripping is much greater at the working electrode for the cell cycled at 2.5 $mA \cdot cm^{-2}$ under 7 MPa pressure reaching the voltage limit of 3 V after 17 cycles, whereas stripping polarisation is greater at the counter for the cell cycled at 1.5 $mA \cdot cm^{-2}$ under 4 MPa pressure, reaching the voltage limit of 3 V after only 11 cycles whereas the voltage at the working electrode only reaches 0.44 V. It is clear that although contact loss is occurring on stripping on both electrodes, it is not occurring at the same rate. We anticipated that the electrode stripped first was most likely to have the greatest initial contact loss, however other factors such as a higher concentration of initial voids or a higher concentration of ionically insulating surface species may dominate in determining the relative rate of contact loss over multiple cycles and hence dominant contact loss at both working and counter electrodes is observed in different cells.

2.4. Critical pressure with current density

To investigate the functional relationship between pressure and void formation at different current densities, five 3-electrode cells were constructed and the polarisation increase with pressure on stripping at different current densities measured, (Fig 6). The cells were placed under a known pressure and the potential increase measured following 0.1 $mA \cdot h \cdot cm^{-2}$ charge passed. Following this, the cells were placed under high pressure (15 MPa) to reform the interface before being placed at a lower known pressure and the potential

increase at different current densities determined again. This was repeated, reducing the pressure in steps of approximately 1 MPa until the increase in potential exceeded 3 V. These data show that the dependence of voltage increase on pressure has the same functionality regardless of current density, with the curves being displaced to higher pressures for higher current densities. Each curve shows a severe variation of polarisation with increase in pressure, Fig. 6.

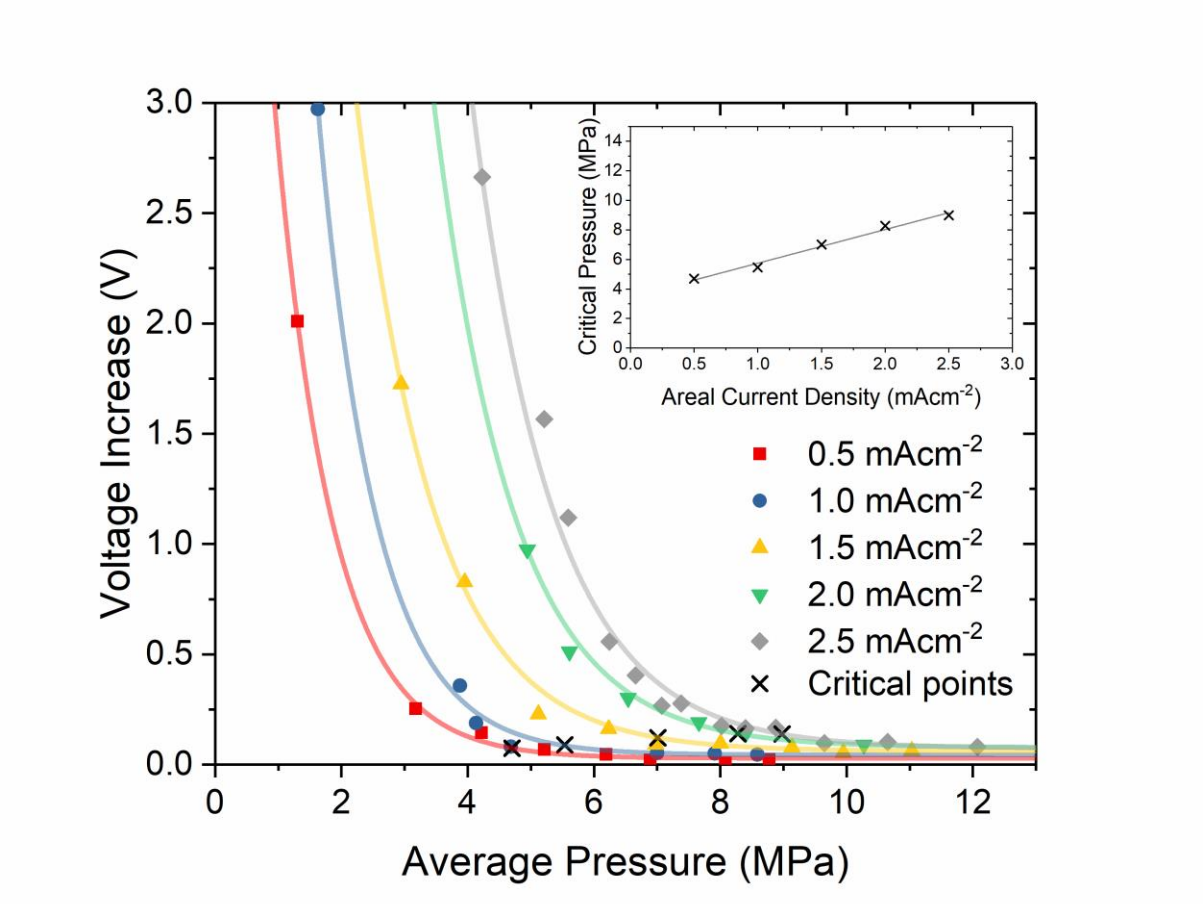

Figure 6: Figure showing the functionality between average pressure and voltage increase at 0.5, 1.0, 1.5, 2.0 and 2.5 mA·cm^{-2} areal current densities. The inset shows how the critical pressure varies with areal current density.

Voids form when the flux of Na^+ ions away from the interface exceeds the flux of Na to the interface due to Na diffusion and creep. The variation with pressure suggests that creep (stress-driven deformation) is the

major mechanism of Na transport to the interface. For each current density, the critical pressure required to suppress void formation was estimated as described in the Methods and these are plotted in the inset of Figure 6. This shows that the critical pressure required for the suppression of voids increases linearly with current density; the flux of Na to the interface is linearly dependent on pressure. Based on the comparison of Na/Na-β"-alumina and Li/Li_6PS_5Cl and recognising that other factors may also play a role, it appears that higher current densities are possible with Na anodes likely due to a greater creep rate.[20]

A 2-electrode cell was constructed and cycled under 4 MPa pressure, at a current density of 0.1 mA·cm^{-2} which is predicted to mitigate voiding. This was confirmed with highly reversibly cycling over 100 cycles (Supplementary Figure 5). Given that sufficiently high pressures can increase the rate of creep and so maintain good interfacial contact regardless of current density, is it possible to enable very high current densities by using very high external pressures? As seen in Figure 7, a single plating of a 3-electrode cell at a current density of 3.0 mA·cm^{-2} was observed to lead to dendrite growth, irrespective of whether the pressure was 4 MPa (Fig 7a) or 12 MPa (Fig 7b). Therefore, it is not possible to operate a cell at ever higher current densities simply by increasing pressure.

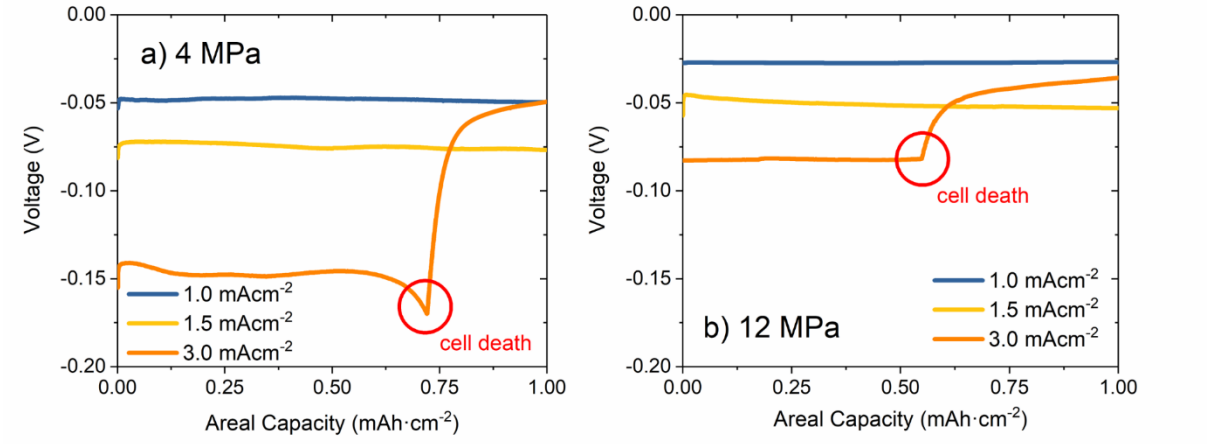

Figure 7: Potential between the working and reference electrodes for a single plating at 1.0, 1.5 and 3.0 mA·cm^{-2} when a) at 4.0 MPa and b) at 12.0 MPa.

This is in agreement with the existence of 2 critical current densities; that on stripping (CCS) which we have already discussed, and that on plating (CCP) which is defined as the critical current for dendrite formation on plating. Although the current density at which a cell can operate without forming voids can be increased using external pressure, even when a 100 % conformal interface is maintained, if the overall current density is above the critical current for plating (CCP) dendrites will form and this acts as the ultimate power limit of an ASSB. However, at more modest and arguably more practical pressures, CCS is usually less than CCP and hence CCS sets the upper limit for the current density at which an ASSB can operate. Values of CCS are not considered to be truly intrinsic due to possible differences in the extent of passivating (insulating) layers at the interface. If a cell initially has a smaller area of direct Na/SE contact due to surface contamination, then it will have a higher current density at the interface for the same overall current density. To emphasise this, Supplementary Figure 6 shows the significant difference in observed critical current density between a disk heated at 400 °C following polishing, i.e. the protocol used in this paper (short circuit occurs at 3.0 $mA \cdot cm^{-2}$) and an untreated disk (short circuit occurs at 0.5 $mA \cdot cm^{-2}$) of Na-β''-alumina.

Whereas CCS is not an intrinsic value, there will exist a critical overpotential of stripping that leads to void formation which is intrinsic. For example, if only 25 % of the SE is actually in contact with the Na electrode, the CCS will be a quarter of the value compared to a case where there was 100 % contact. On the other hand, the overpotential in these two cases will be the same and therefore is a better predictor of cell failure. However, since current density is a direct measure of flux of Na^+ away from the interface, we have used critical current rather than critical overpotential due to the kinetic treatment of interfacial processes in this study.

3. Conclusion

The Na/Na-β''-alumina interface exhibits formation of voids in the Na anode at the interface on stripping, which accumulate on cycling leading to dendrites on plating, short circuit and cell failure. This

occurs above a critical stripping current (CCS), which is a linear function of stack pressure, consistent with Na creep being the dominant mechanism of Na transport to the interface. It requires pressures of several MPa to avoid cell death when cycled at current densities of several $mA \cdot cm^{-2}$ at room temperature, > 9 MPa at 2.5 $mA \cdot cm^{-2}$. Solutions to increase the rate of Na creep to the interface may be required in practical cells if they are to be operated at high rates, such as increasing the temperature of cell operation or designing anodes with more favourable mechanical properties by alloying Na metal.

4. Methods

4.1. Preparation of Na-β''-alumina discs

Discs of Na-*β''*-alumina of diameter 10 mm and thickness 0.7 mm were purchased from Ionotec. The density of these discs was determined by comparison of the envelope density determined by 7 cycles using a micrometrics GeoPyc 1360 Envelope and T.A.P. Density Analyser, to the measured crystal density determined by 10 cycles on a micrometrics AccuPyc II 1340 Gas Pycnometer. The discs were polished in deionised water on successively finer grits of SiC paper (400, 600, 800, 1200, 2500). They were then dried and transferred into an Ar filled glovebox (O_2 and H_2O level < 1 ppm) where they were heat treated at 400 °C in a platinum crucible prior to use. The procedure is adapted from that employed previously for the treatment of LLZO surfaces by Sakamoto and co-workers.[29]

4.2. Na/Na-β''-alumina/Na cell assembly

Within an Ar filled glovebox, Na metal was cut from ingot and any surface film removed carefully using a scalpel. The Na metal was then pressed against an Al spacer of 5 mm diameter to form an approximately 100 μm thick Na electrode, which was then cut to size. These 5 mm discs of Na were used as working and counter electrodes. A 1 mm diameter reference electrode was prepared similarly to complete the 3-electrode cells. Polypropylene masks were used to prevent lateral spread of Na under pressure. The 3-electrode cell is shown in Fig S2. The cells were sealed under vacuum in a pouch cell with aluminium foil current collectors.

Spring clamps and a piezoelectric load cell (OMEGA), or a 5 kN stage (Deben) loading rig was used to measure pressure. The latter was used to compress the cell, giving continuous readings of the applied pressure.

4.3. X-ray Photoelectron Spectroscopy

XPS was performed using an ion-pumped ultrahigh-vacuum chamber fitted with a VG nine-channel CLAM4 electron energy analyser. The sample was transferred to the XPS chamber from an Ar filled glovebox using a custom airtight transfer device. Data were corrected relative to the C 1s signal of adventitious carbon (284.8 eV)

4.4. Galvanostatic Cycling and PEIS

Constant pressure galvanostatic cycling was carried out using a Bio-Logic MPG2 potentiostat. All galvanostatic cycling was conducted at room-temperature.

PEIS was performed on 2-electrode cells with a voltage perturbation of 10 mV in a frequency range from 1 MHz to 1 Hz on a Gamry Interface-1010E potentiostat. The data were fitted for analysis using the ZView software package.

4.5. Scanning electron microscopy

Cells were cross-sectioned using a Sonotec ultrasonic cutter with a tungsten carbide blade in an Ar filled glovebox. The fractured discs were mounted in a custom-built holder using Cu adhesive tape and transferred to be imaged in a Zeiss Merlin SEM using an air-tight transfer device (Gatan).

4.6. X-ray computed tomography

3-electrode pouch cells were mounted within a Deben CT5000 loading rig which was operated inside a Zeiss Xradia Versa 510 X-ray computed tomography microscope. In situ tomographs were recorded at 120 kV accelerating voltage with an image voxel dimension of 2.2048 μm.

The quantitative analysis was conducted using Avizo Fire. The 16bit Hounsfield grayscale image was filtered with non-local means filter first, then with the voids segmented out with interactive thresholding, and quantitatively analysed by label analysis.

4.7. Estimating critical pressures

Critical pressures were estimated based on the fitted data shown in Figure 6. For each set of data obtained at a different current density, the derivative of the fitted function was taken. The critical pressure was estimated to be the pressure at which $dV/dP = -0.05$. This value was chosen as being within the margin of error of the horizontal, high pressure region of the curve.

ASSOCIATED CONTENT

Supplementary figures (PDF)

Supplementary Information includes XPS and PEIS before and after Na-β''-alumina surface treatment, a schematic of the 3-electrode cell, SEM images under additional cycling conditions, 2-electrode cycling data at low current density and rate tests for treated and untreated Na-β''-alumina discs.

AUTHOR INFORMATION

Corresponding Author

*Email:peter.bruce@materials.ox.ac.uk

Author Contributions

D.S.J. contributed to all aspects of the research. Z.N. carried out in-situ tomography experiments. J.E.D. devised and operated the set-up for pressure application. D.S.J., Z.N., J.K., G.O.H., P.A., J.M., D.E.J.A. and P.G.B. interpreted the data. D.S.J. and P.G.B. wrote the paper. The project was supervised by P.G.B.

ACKNOWLEDGMENT

P.G.B. is indebted to the Faraday Institution [FIRG007, FIRG008], The Engineering and Physical Sciences Research Council (EPSRC), including the SUPERGEN Energy Storage Hub [EP/L019469/1] and the Sir Henry Royce Institute for financial support [EP/R010145/1]. The X-ray tomography facilities were funded by EPSRC Grant [EP/M02833X/1] "University of Oxford:

experimental equipment upgrade". The authors thank Dr. Phil Holdway, Oxford Materials Characterisation Service, for help with XPS measurements.

REFERENCES

(1) Hooper, A.; Tofield, B. C. All-Solid-State Batteries. *J. Power Sources* **1984**, *11*, 33–41.

(2) Kerman, K.; Luntz, A.; Viswanathan, V.; Chiang, Y.-M.; Chen, Z. Review—Practical Challenges Hindering the Development of Solid State Li Ion Batteries. *J. Electrochem. Soc.* **2017**, *164* (7), A1731–A1744.

(3) Lotsch, B. V.; Maier, J. Relevance of Solid Electrolytes for Lithium-Based Batteries: A Realistic View. *J. Electroceramics* **2017**, *38* (2–4), 128–141.

(4) Famprikis, T.; Canepa, P.; Dawson, J. A.; Islam, M. S.; Masquelier, C. Fundamentals of Inorganic Solid State Electrolytes for Batteries. *Nat. Mater.* **2019**.

(5) Janek, J.; Zeier, W. G. A Solid Future for Battery Development. *Nat. Energy* **2016**, *1* (9), 16141.

(6) Linden, E.; Reddy, T. B. *Handbook of Batteries*; McGraw-Hill, New York, 2001.

(7) Haas, R.; Pompe, C.; Osenberg, M.; Hilger, A.; Manke, I.; Mogwitz, B.; Maitra, U.; Langsdorf, D.; Schröder, D. Practical Implications of Using a Solid Electrolyte in Batteries with a Sodium Anode: A Combined X-Ray Tomography and Model-Based Study. *Energy Technol.* **2019**, *7* (7), 1–8.

(8) Porz, L.; Swamy, T.; Sheldon, B. W.; Rettenwander, D.; Frömling, T.; Thaman, H. L.; Berendts, S.; Uecker, R.; Carter, W. C.; Chiang, Y. M. Mechanism of Lithium Metal Penetration through Inorganic Solid Electrolytes. *Adv. Energy Mater.* **2017**, *7* (20), 1–12.

(9) Swamy, T.; Park, R.; Sheldon, B. W.; Rettenwander, D.; Porz, L.; Berendts, S.; Uecker, R.; Carter, W. C.; Chiang, Y.-M. Lithium Metal Penetration Induced by Electrodeposition

through Solid Electrolytes: Example in Single-Crystal $Li_6La_3ZrTaO_{12}$ Garnet. *J. Electrochem. Soc.* **2018**, *165* (16), A3648–A3655.

(10) Monroe, C.; Newman, J. Dendrite Growth in Lithium/Polymer Systems. *J. Electrochem. Soc.* **2003**, *150* (10), A1377.

(11) Monroe, C.; Newman, J. The Impact of Elastic Deformation on Deposition Kinetics at Lithium/Polymer Interfaces. *J. Electrochem. Soc.* **2005**, *152*, A396.

(12) Cheng, E. J.; Sharafi, A.; Sakamoto, J. Intergranular Li Metal Propagation through Polycrystalline $Li_{6.25}Al_{0.25}La_3Zr_2O_{12}$ Ceramic Electrolyte. *Electrochim. Acta* **2017**, *223*, 85–91.

(13) Krauskopf, T.; Dippel, R.; Hartmann, H.; Peppler, K.; Mogwitz, B.; Richter, F. H.; Zeier, W. G.; Janek, J. Lithium-Metal Growth Kinetics on LLZO Garnet-Type Solid Electrolytes. *Joule* **2019**, *3* (8), 2030–2049.

(14) Marbella, L. E.; Zekoll, S.; Kasemchainan, J.; Emge, S. P.; Bruce, P. G.; Grey, C. P. ^{7}Li NMR Chemical Shift Imaging to Detect Microstructural Growth of Lithium in All-Solid-State Batteries. *Chem. Mater.* **2019**, *31* (8), 2762–2769.

(15) Manalastas, W.; Rikarte, J.; Chater, R. J.; Brugge, R.; Aguadero, A.; Buannic, L.; Llordés, A.; Aguesse, F.; Kilner, J. Mechanical Failure of Garnet Electrolytes during Li Electrodeposition Observed by In-Operando Microscopy. *J. Power Sources* **2019**, *412*, 287–293.

(16) Pang, Q.; Zhou, L.; Nazar, L. F. Elastic and Li-Ion–Percolating Hybrid Membrane Stabilizes Li Metal Plating. *Proc. Natl. Acad. Sci. U. S. A.* **2018**, *115* (49), 12389–12394.

(17) Fang, C.; Wang, X.; Meng, Y. S. Key Issues Hindering a Practical Lithium-Metal Anode. *Trends Chem.* **2019**, *1* (2), 152–158.

(18) Wang, M. J.; Choudhury, R.; Sakamoto, J. Characterizing the Li-Solid-Electrolyte Interface Dynamics as a Function of Stack Pressure and Current Density. *Joule* **2019**, 1–14.

(19) Koshikawa, H.; Matsuda, S.; Kamiya, K.; Miyayama, M.; Kubo, Y.; Uosaki, K.; Hashimoto, K.; Nakanishi, S. Dynamic Changes in Charge-Transfer Resistance at Li Metal/$Li_7La_3Zr_2O_{12}$ interfaces during Electrochemical Li Dissolution/Deposition Cycles. *J. Power Sources* **2018**, *376*, 147–151.

(20) Kasemchainan, J.; Zekoll, S.; Spencer Jolly, D.; Ning, Z.; Hartley, G. O.; Marrow, J.; Bruce, P. G. Critical Stripping Current Leads to Dendrite Formation on Plating in Lithium Anode Solid Electrolyte Cells. *Nat. Mater.* **2019**, *18*, 1105–1111.

(21) Krauskopf, T.; Hartmann, H.; Zeier, W. G.; Janek, J. Toward a Fundamental Understanding of the Lithium Metal Anode in Solid-State Batteries - An Electrochemo-Mechanical Study on the Garnet-Type Solid Electrolyte $Li_{6.25}Al_{0.25}La_3Zr_2O_{12}$. *Appl. Interfaces Mater.* **2019**, No. 11, 14463–14477.

(22) Masias, A.; Felten, N.; Garcia-mendez, R.; Wolfenstine, J.; Sakamoto, J. Elastic, Plastic, and Creep Mechanical Properties of Lithium Metal. *J. Mater. Sci.* **2019**, *54* (3), 2585–2600.

(23) Wenzel, S.; Leichtweiss, T.; Weber, D. A.; Sann, J.; Zeier, W. G.; Janek, J. Interfacial Reactivity Benchmarking of the Sodium Ion Conductors Na_3PS_4 and Sodium β-Alumina for Protected Sodium Metal Anodes and Sodium All-Solid-State Batteries. *ACS Appl. Mater. Interfaces* **2016**, *8* (41), 28216–28224.

(24) Wu, T.; Wen, Z.; Sun, C.; Wu, X.; Zhang, S.; Yang, J. Disordered Carbon Tubes Based on Cotton Cloth for Modulating Interface Impedance in β-Al_2O_3-Based Solid-State Sodium Metal Batteries. *J. Mater. Chem.. A* **2018**, No. 6, 12623–12629.

(25) Lacivita, V.; Wang, Y.; Bo, S. H.; Ceder, G. Ab Initio Investigation of the Stability of Electrolyte/Electrode Interfaces in All-Solid-State Na Batteries. *J. Mater. Chem. A* **2019**, *7* (14), 8144–8155.

(26) De Jonghe, C.; Feldman, L.; Buechele, A. Failure Modes of Na-Beta Alumina. *Solid State Ionics* **1981**, *5*, 267–270.

(27) De Jonghe, L. C.; Feldman, L.; Beuchele, A. Slow Degradation and Electron Conduction in Sodium/Beta-Aluminas. *J. Mater. Sci.* **1981**, *16* (3), 780–786.

(28) Richman, R. H.; Tennenhouse, G. J. A Model for Degradation of Ceramic Electrolytes in Na-S Batteries. *J. Am. Ceram. Soc.* **1975**, *58* (1–2), 63–67.

(29) Sharafi, A.; Kazyak, E.; Davis, A. L.; Yu, S.; Thompson, T.; Siegel, D. J.; Dasgupta, N. P.; Sakamoto, J. Surface Chemistry Mechanism of Ultra-Low Interfacial Resistance in the Solid-State Electrolyte $Li_7La_3Zr_2O_{12}$. *Chem. Mater.* **2017**, *29* (18), 7961–7968.

(30) Wang, M.; Sakamoto, J. Correlating the Interface Resistance and Surface Adhesion of the Li Metal-Solid Electrolyte Interface. *J. Power Sources* **2018**, *377*, 7–11.

(31) Sharafi, A.; Yu, S.; Naguib, M.; Lee, M.; Ma, C.; Meyer, H. M.; Nanda, J.; Chi, M.; Siegel, D. J.; Sakamoto, J. Impact of Air Exposure and Surface Chemistry on Li-$Li_7La_3Zr_2O_{12}$ Interfacial Resistance. *J. Mater. Chem. A* **2017**, *5* (26), 13475–13487.

(32) Han, X.; Gong, Y.; Fu, K.; He, X.; Hitz, G. T.; Dai, J.; Pearse, A.; Liu, B.; Wang, H.;

Rubloff, G.; Mo, Y.; Thangadurai, V.; Wachsman, E.D.; Hu, L. Negating Interfacial Impedance in Garnet-Based Solid-State Li Metal Batteries. *Nat. Mater.* **2017**, *16* (5), 572–579.

TOC Graphic:

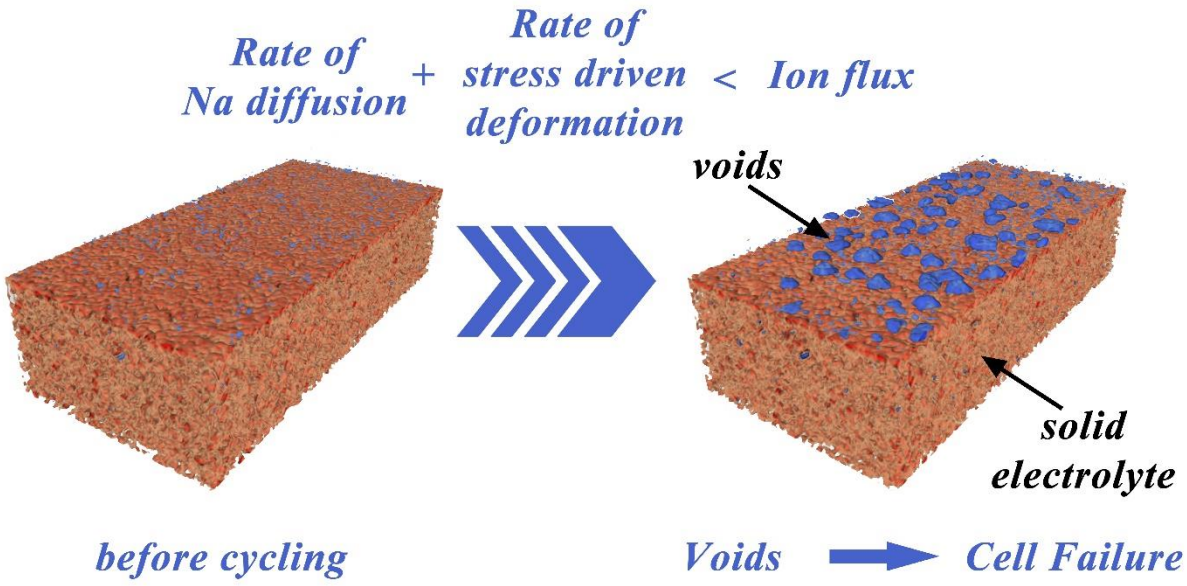
Rate of
Na diffusion
+
Rate of
stress driven
deformation
<
Ion flux
voids
solid
electrolyte
before cycling
Voids
Cell Failure